International Communications in Heat and Mass Transfer 151 (2024) 107212

Contents lists available at ScienceDirect

International Communications in Heat and Mass Transfer

journal homepage: www.elsevier.com/locate/ichmt

Optimizing heat flow: Nano-encapsulated phase change materials in vibration-enhanced gravity-driven thermal convection

Nidhal Ben Khedher [a,b], S.A.M. Mehryan [c,*], Ahmad Hajjar [d], Abed Saif Alghawli [e], Mohammad Ghalambaz [f,*], Kasra Ayoubi Ayoubloo [g], Sami Dhahbi [h]

[a] *Department of Mechanical Engineering, College of Engineering, University of Ha'il, 81451 Ha'il City, Saudi Arabia*
[b] *Laboratory of Thermal and Energetic Systems Studies (LESTE) at the National School of Engineering of Monastir, University of Monastir, Tunisia*
[c] *Young Researchers and Elite Club, Yasooj Branch, Islamic Azad University, Yasooj, Iran*
[d] *Center for Environmental Intelligence and College of Engineering and Computer Science, VinUniversity, Hanoi, Viet Nam*
[e] *Department of Computer Science, College of Computer Engineering and Sciences, Prince Sattam bin Abdulaziz University, Al-Kharj 11942, Saudi Arabia*
[f] *Laboratory on Convective Heat and Mass Transfer, Tomsk State University, 634050 Tomsk, Russia*
[g] *Department of Mechanical Engineering, Shahid Chamran University of Ahvaz, Ahvaz, Iran*
[h] *Department of Computer science, College of Science and Art at Mahayil, King Khalid University, Muhayil Aseer 62529, Saudi Arabia*

ARTICLE INFO

Keywords:
Mechanical vibration
Nano-encapsulated phase change material
Vibrational Rayleigh number
Stefan number
Melting temperature

ABSTRACT

In cavities differentially heated at the sides and subjected to mechanical vibration, the natural convection incoming from buoyancy effects is not the only factor affecting the flow dynamic and heat transfer. The current work aims to address vibrational convection in a square chamber filled with a Nano-Encapsulated Phase Change Material (NEPCM) suspension. The non-dimensional equations of fluid and heat flows in the cavity are developed and solved numerically. The gravity term in the momentum equation is modified to include the effect of vibration. It is shown that the vibrational Rayleigh number has the most effect on the convective heat transfer, followed by the conductivity of the NEPCM suspension. Increasing the vibrational Rayleigh number from 10^3 to 10^7 leads to up to 3 times rise in the time-averaged Nusselt number. The NEPCM concentration has a moderate influence, as around 12% increase in the time-averaged Nusselt number is found when a 5% volume fraction of particles is employed. An increase in the Stefan number from 0.2 to 0.8 is associated with a 6.1% reduction in the time-averaged Nusselt number. Additionally, the peak heat transfer is achieved at the melting point of 0.5, with a 6.5% increase compared to the melting temperature of 0.1.

1. Introduction

In recent years, effective energy management has emerged as a significant challenge in various applications, ranging from residential and industrial cooling systems to energy storage in different systems, and waste heat recovery [1–4]. As a result, intensive research efforts have been directed toward discovering and developing novel, and efficient solutions for energy management [5–7]. Phase Change Materials (PCMs) offer a versatile solution for thermal energy storage and management, finding applications in diverse fields where temperature control and energy efficiency are crucial [8]. One promising avenue that has gained significant traction in heat transfer is the utilization of nano-encapsulated phase change materials (NEPCMs) [9,10].

NEPCMs are microscopic capsules housing a PCM. These materials can absorb or release a substantial amount of latent heat during phase changes, typically transitioning from solid to liquid or vice versa. When these PCMs are reduced to nanoscale dimensions and encapsulated, they provide an increased surface-to-volume ratio, resulting in improved heat transfer efficiency [11]. The thermophysical properties of NEPCMs and the potential of tailoring these properties to match specific application needs have made them a compelling area of study in thermal energy management [10,12,13].

Various recent studies have focused on the utilization of NEPCMs for enhancing heat transfer. Hashemi-Tilehnoee et al. [14] utilized the finite volume method to investigate the heat transfer and free convective flow of NEPCM-water suspension in a hot porous cavity. The research emphasized the roles of the magnetic field, Darcy number, and laminar

---

* Corresponding authors.
E-mail addresses: alal171366244@gmail.com (S.A.M. Mehryan), m.ghalambaz@gmail.com (M. Ghalambaz).

https://doi.org/10.1016/j.icheatmasstransfer.2023.107212

Nomenclature

Latin symbols

b	Amplitude of vibration (m)
Cr	Heat capacity ratio
C_p	Sensible heat capacity ($Jkg^{-1}K^{-1}$)
f	Rectangular function
g	Gravity acceleration (ms^{-2})
H	Size of the square cavity (m)
k	Thermal conductivity ($Wm^{-1}K^{-1}$)
L_{sf}^{*}	Latent heat of the NEPCM core ($kJkg^{-1}$)
Nc	Thermal conductivity number
Nv	Dynamic viscosity number
Nu	Nusselt number
p	Pressure (Pa)
Pr	Prandtl number
Ra_g	Gravity Rayleigh number
Ra_Ω	Vibration Rayleigh number
Ste	Stefan number
T	Temperature (K)
t^{*}	Time (s)
$\vec{u}$	Velocity vector ms^{-1}
u, v	Components of velocity vector along x and y axes (m)
x, y	Cartesian coordinates (m)

Greek symbols

β	Thermal expansion coefficient (K^{-1})
∇	Gradient vector (m^{-1})
ε	Ratio of the heat capacity of NEPCM particles to the base liquid
Ω	Angular frequency of the vibration (s^{-1})
μ	Dynamic viscosity (Nsm^{-2})
ν	Kinematic viscosity (m^2s^{-1})
ρ	Density (kgm^{-3})
ζ	Weight ratio of nanoparticles core to shell
ξ	Ordinary frequency of the vibration (s^{-1})
ϕ	Volume fraction of the nanoparticles

Subscripts

bl	Base liquid
c	Cold wall/ Core of nano-sized particles
initial	Initial condition
h	Hot wall
s	Shell of nano-sized particles
steady	Steady state
Mr	Melting temperature window
m	Melting point/ mean value
na	Nano-sized particles
nl	Nanoliquid
r	properties ratio of the nanoliquid to the base liquid
t,a	Time-averaged value

Superscript

*	Dimensional properties and parameters

Abbreviations

FEM	Finite element method
NEPCM	Nano-encapsulated phase change material
PDE	Partial differential equation

Rayleigh number on the flow and heat transfer characteristics. It was observed that the heat transfer capability of the cavity containing the NEPCM-water suspension was superior, particularly at lower Rayleigh numbers. Concurrently, [15,16] explored the role of double-diffusive convection in the heat transfer of NEPCM suspensions within cavities of different shapes. Both studies employed the incompressible smoothed particle hydrodynamics ISPH method. They noted that the fusion temperature of the NEPCM played a significant role in determining the phase change zone and its intensity within the cavities. In [16], it was further demonstrated that parameters, such as the buoyancy ratio and Darcy parameters, were pivotal in controlling the distribution of solid particles within the nanofluid phase. Hussain et al. [17] built on these observations by analyzing the natural convection of NEPCM within a porous grooved cavity. In this study, the effect of parameters such as porosity, Darcy parameter, and Rayleigh number on the nanofluid flow and convective heat transfer were scrutinized. Their conclusion highlighted that alterations in these parameters had profound impacts on the streamlines and heat capacity patterns within the grooved cavity.

Meanwhile, [18,19] extended the applications of NEPCM to more complex geometries and boundary conditions. They discovered that changes in the shape, size, and rotation of internal objects had considerable impacts on heat and mass transport inside the cavities. However, Raizah and Aly [18] observed that thermal performance could be enhanced by including solid particles into the phase change material.

Unique applications of NEPCM, such as bioconvection [20] and fuel cells [21], have been explored. Hussain et al. [20] focused on the bioconvection of oxytactic microorganisms in an omega-shaped porous enclosure suspended by NEPCM, while [21] examined the use of NEPCM in cooling polymer electrolyte membrane fuel cells. Both studies emphasized NEPCM's ability to control heat transfer and storage. In [22], the effect of radiation on the heat transfer and fluid flow of NEPCM in prismatic enclosures was studied. The findings revealed that the radiation parameter influences the melting/solidification processes, and the use of NEPCM particles significantly improved heat transfer. Besides, Alazzam et al. [23] analyzed the natural convection characteristics of NEPCM-water mixture in a cubic enclosure under an external magnetic field, emphasizing how the magnetic field and various other parameters influenced heat transfer.

Vibration is a mechanical phenomenon characterized by oscillations or back-and-forth movements of an object or a medium. It is a result of a periodic disturbance or a force applied to a system, causing it to move repetitively around a central equilibrium position [24,25]. Highlighting the critical influence of vibrations on heat transfer in enclosures, some studies have demonstrated the complex interplay between these two variables and the varying parameters that come into play. The concept of vibrations enhancing the heat transfer rates within a rectangular enclosure is exhibited by the experimental study carried out [26]. Applying forced vibration conditions demonstrated that high heat transfer could be achieved at frequencies near the system's natural frequency under constant heat flux. However, it is crucial to carefully select the heat flux and frequency ratio to maximize heat transfer parameters while minimizing power consumption. In a similar vein, a significant increase in convective heat transfer coefficients was found when the enclosure was subjected to vibrations, especially near the natural resonant frequency of the fluid column within the enclosure [27]. This aligns with the findings indicating that resonance occurs when the oscillation frequency matches the basic mode of internal gravity oscillations, thereby intensifying convective activities [28].

Adding another layer to this understanding, studies have explored the impact of additional variables on the vibrational heat transfer process. The combined effects of mechanical variation and an applied magnetic field have been explored, demonstrating the effectiveness of the magnetic field in stabilizing the system and thereby reducing flow moments [29]. Similar results were observed in another study where an externally imposed magnetic field had a stabilizing impact on thermo-vibrational convective instability in an anisotropic porous module permeated by a second-grade fluid [30]. Furthermore, the study provided insights into the effects of anisotropies on the permeability and thermal diffusivity of the porous module along the transverse direction.

Complementing this, the introduction of mechanical vibrations and magnetic fields in an enclosure resulted in a uniform oscillation generation and a decrease in the amplitude of the Nusselt number oscillation with increasing magnetic field strength [31]. Moreover, numerical simulations showed the potential for significant improvements in heat transfer mechanisms by applying mechanical vibrations driven by an eccentrically connected electric motor to an air-filled square cavity [32].

Vibration has also been found to influence the onset of thermo-solutal convection in a confined porous cavity saturated by a binary mixture [33]. Similarly, another study discovered that vertical vibrations could decrease the flow intensity and fluid penetration into a porous section of an enclosure, impacting both heat and mass transfer rates [34]. Furthermore, a hybrid nanofluid in a square cavity subjected to gravitational and vibrational forces exhibited an amplified rate of heat transfer for all studied frequencies, suggesting that the composition of the medium within the enclosure could play a role [35].

In the expansive domain of thermal sciences, the intricate nexus between vibrations and heat transfer has been a focal point of numerous scholarly inquiries. A substantial body of literature substantiates the constructive impact of vibrations on heat transfer within confined environments. This intricate thermal interplay, however, is contingent upon a myriad of factors, encompassing the frequency and amplitude of vibrations, intrinsic physical characteristics of the enclosure, and the working fluid composition. NEPCM particles present a cutting-edge paradigm within this milieu, harnessing the latent heat of nanoparticles to intricately augment heat transfer processes. Consequently, this research embarks on a systematic exploration of the convective heat transfer dynamics inherent in NEPCM suspensions within a vibrated cavity. The purpose of this research is to contribute novel insights to the field of convective heat transfer within enclosures, specifically focusing on the interaction between NEPCMs and mechanical vibrations. In pursuit of our objective, we employ a numerical approach to solve the non-dimensionalized fundamental equations of the flow and heat transfer within a vibrated cavity hosting NEPCM particles. To gauge the robustness of our findings, we scrutinize the influence of computing mesh size on the results. Additionally, we validate our results by comparing them with findings documented in the existing literature. Moving beyond validation, we systematically explore the impact of various parameters on the flow dynamics and heat transfer rate.

2. Physical model

The objective of this work is to examine the convection flow occurring within a two-dimensional square capsule filled with an aqueous liquid containing particles of NEPCM. Fig. 1 illustrates the visual representation of the capsule configuration under investigation. The cavity experiences a vertical and sinusoidal vibration, indicating periodic variations in the buoyancy force along the vertical direction. The sinusoidal vibrations within the cavity are defined by their amplitude, represented as b^*, and frequency, denoted as Ω^*. Consequently, the instantaneous acceleration is composed of a constant term, g^*, and a time-varying component, $b^*\Omega^{*2}sin(\Omega^* t^*)$. The size of the square capsule is H^*. The cold wall of the enclosure is maintained at a constant temperature, denoted as T_c^*, while the hot wall is set to a temperature of T_h^*. The lower and upper horizontal surfaces are treated as adiabatic in the analysis, meaning that there is no heat transfer occurring through these walls. The dispersion of particles within the host liquid is uniform, ensuring a homogeneous distribution. Additionally, thermal and dynamic balances are achieved between the particles and the host liquid. The assumptions made for the analysis include the fluid being Newtonian, and the flow is characterized as laminar. The amplitude of the vibration velocity, denoted as $b^*\Omega^*$, is assumed to be relatively small, and the flow is considered incompressible. The validity of the Boussinesq approximation is assumed, and the effect of radiation is disregarded for the analysis.

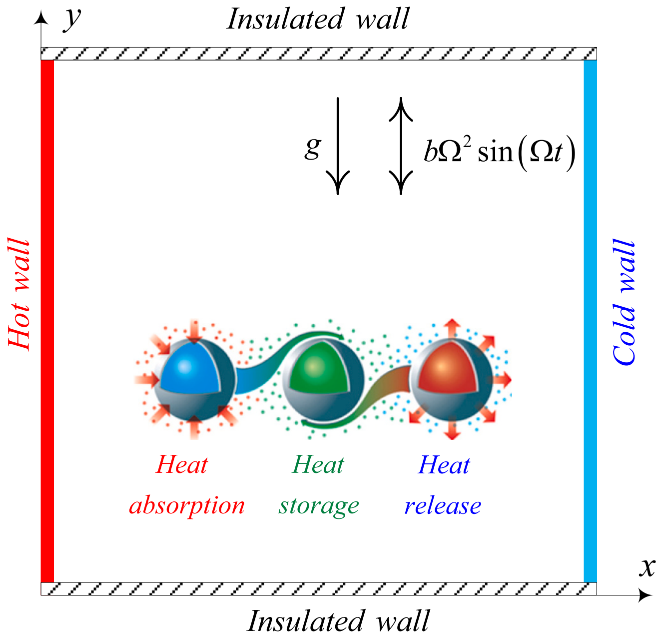

Fig. 1. Schematic representation of the physical domain.

3. Conservation equations, boundary conditions, and properties of nanoliquid

Describing the dynamics and thermal aspects, the equations shaping the flow and temperature fields are outlined below [36]:

Mass conservation:

$$\nabla^* . \overrightarrow{\boldsymbol{u}}^* = 0 \tag{1}$$

Momentum conservation:

$$\rho_{nl}^* \frac{\partial \overrightarrow{\boldsymbol{u}}^*}{\partial t^*} + \rho_{nl}^* \overrightarrow{\boldsymbol{u}}^* . \nabla^* \overrightarrow{\boldsymbol{u}}^* = -\nabla^* p^* + \mu_{nl}^* \nabla^{*2} \overrightarrow{\boldsymbol{u}}^* + \left(g^* + b^* \Omega^{*2} sin(\Omega^* t^*)\right) \rho_{nl}^* \beta_{nl}^* \left(T_{nl}^* - T_c^*\right) \overrightarrow{\boldsymbol{j}} \tag{2}$$

Here, Ω^*, as the angular frequency, is $2\pi\xi^*$, where ξ^* is the ordinary frequency. ρ_{nl}^* is the density of nanoliquid, $\overrightarrow{\boldsymbol{u}}^*$ is the velocity vector, t^* is time, p^* is the pressure, μ_{nl}^* is the dynamic viscosity, g^* is the gravity acceleration, b^* is the vibration amplitude, β_{nl}^* is the volume-thermal expansion coefficient, and T_{nl}^* is temperature.

Energy conservation:

$$\rho_{nl}^* C_{p,nl}^* \frac{\partial T_{nl}^*}{\partial t^*} + \rho_{nl}^* C_{p,nl}^* \overrightarrow{\boldsymbol{u}}^* . \nabla^* T_{nl}^* = k_{nl}^* \nabla^{*2} T_{nl}^* \tag{3}$$

where $C_{p,nl}^*$ and k_{nl}^* are the heat capacity and thermal conductivity of the nanoliquid. Concerning the physical aspects of the problem, the boundary conditions are formulated in the following manner:

$$for \begin{cases} x^* = 0 \\ 0 \leq y^* \leq H^* \end{cases} \Rightarrow \overrightarrow{\boldsymbol{u}}^* = 0, T^* = T_h^* \tag{4-a}$$

$$for \begin{cases} x^* = H^* \\ 0 \leq y^* \leq H^* \end{cases} \Rightarrow \overrightarrow{\boldsymbol{u}}^* = 0, T^* = T_h^* \tag{4-b}$$

$$for \begin{cases} y^* = 0 \\ y^* = H^* \\ 0 \le x^* \le H^* \end{cases} \Rightarrow \overrightarrow{\boldsymbol{u}}^* = 0, \frac{\partial T^*}{\partial y^*} = 0 \tag{4-c}$$

Additionally, the initial condition is:

$$for \begin{cases} 0 < x < H^* \\ 0 < y < H^* \Rightarrow \overrightarrow{\boldsymbol{u}}^* = \overrightarrow{\boldsymbol{u}}^*_{steady}, T^* = T^*_{steady} \\ t^* = 0 \end{cases} \tag{4-d}$$

The thermophysical characteristics of the NEPCM nanoliquid, as outlined in eqs. (5)–(9), are presented below:

The nanoliquid density is:

$$\rho^*_{nl} = \rho^*_{na}\phi + \rho^*_{bl}(1-\phi) \tag{5-a}$$

$$\rho^*_{na} = (1+\zeta)\left(\rho^*_s + \iota\rho^*_c\right)^{-1}\rho^*_c\rho^*_s \tag{5-b}$$

ρ^*_{na} is the density of the nano-sized particles, ρ^*_{bl} is the density of the host liquid, and ϕ is the volume fraction of the particles. ρ^*_c and ρ^*_s are the density of the nano-sized particles core and shell, respectively. The weight ratio of nanoparticles core to shell, denoted as ζ in the aforementioned relation, is approximately 0.447. The effective specific heat capacity, expressed as a function of the specific heat capacities of the particles and the host liquid, is as follows:

$$C^*_{p,nl} = \left[\rho^*_{nl}\right]^{-1}\left[\rho^*_{bl}C^*_{p,bl}(1-\phi) + \rho^*_{na}C^*_{p,na,eff}\phi\right] \tag{6}$$

In instances where the core of particles remains unaffected by the phase transition phenomenon, the effective specific heat capacity of particles, i.e., $C^*_{p,na,eff}$, is equivalent to the sensible heat capacity of the particle, i.e., $C^*_{p,na}$, determinable through the relation presented hereafter [23]:

$$C^*_{p,na} = \left[\rho^*_c\rho^*_s C^*_{p,c} + \zeta\rho^*_c\rho^*_s C^*_{p,s}\right]\left[\rho^*_s\rho^*_{na} + \zeta\rho^*_c\rho^*_{na}\right]^{-1} \tag{7}$$

where $C^*_{p,c}$ and $C^*_{p,s}$ are the sensible heat capacity of the core and shell of the nanoparticles, respectively. During the phase transition, the heat capacity of the nanoparticles becomes:

$$C^*_{p,na,eff} = C^*_{p,na} + \left\{\frac{\pi}{2}\cdot\left(\frac{L^*_{sf}}{T^*_{Mr}} - C^*_{p,na}\right)\cdot sin\left(\pi\frac{T^* - T^*_m + T^*_{Mr}/2}{T^*_{Mr}}\right)\right\}\mathrm{I} \tag{8-a}$$

$$\begin{cases} for\ T^* < \left(-T^*_{Mr}/2\right) + T^*_m \Rightarrow I = 0 \\ for - \left(T^*_{Mr}/2\right) + T^*_m < T^* < \left(T^*_{Mr}/2\right) + T^*_m \Rightarrow I = 1 \\ for\ T^* > \left(T^*_{Mr}/2\right) + T^*_m \Rightarrow I = 0 \end{cases} \tag{8-b}$$

L^*_{sf} and T^*_m of the above-written equations are the latent heat and melting temperature of the nanoparticles core. T^*_{Mr} is the melting temperature window. The coefficient of thermal-volume expansion for the nanoliquid is:

$$\beta^*_{nl} = (1-\phi)\beta^*_{bl} + \phi\beta^*_{na} \tag{9}$$

in which, β^*_{bl} and β^*_{na} are, respectively, the thermal-volume expansion coefficients of the host liquid and NEPCM particles.

4. Non-dimensionalized form of the conservation equations

The parameters used for dimensionlessizing the equations and boundary conditions are:

$$\overrightarrow{u} = \frac{H^*}{\left(k^*_{bl}/\rho^*_{bl}C^*_{p,bl}\right)}\overrightarrow{u}^*, p = \frac{H^{*2}}{\rho^*_{bl}\left(k^*_{bl}/\rho^*_{bl}C^*_{p,bl}\right)^2}p^*, T = \frac{T^* - T^*_c}{T^*_h - T^*_c}, \nabla = \frac{\nabla^*}{H^*}$$

$$(\xi, \Omega) = \frac{H^{*2}}{\left(k^*_{bl}/\rho^*_{bl}C^*_{p,bl}\right)}(\xi^*, \Omega^*), (x, y) = \frac{(x^*, y^*)}{H^*}, \tau = \frac{t^*\left(k^*_{bl}/\rho^*_{bl}C^*_{p,bl}\right)}{H^{*2}} \tag{10}$$

where $\overrightarrow{\boldsymbol{u}}$ is the non-dimensionalized velocity vector, p non-dimensionalized pressure, T non-dimensionalized temperature, ∇ non-dimensionalized gradient vector, Ω non-dimensionalized angular frequency, τ non-dimensionalized time, and x (or y) non-dimensionalized coordinate. Applying the non-dimensionalization parameters aforementioned yields the non-dimensionalized forms of the equations:

$$0 = \nabla.\overrightarrow{\boldsymbol{u}} \tag{11}$$

$$\begin{aligned} &-\nabla p + Pr\mu_r\nabla^2\overrightarrow{\boldsymbol{u}} + Ra_g Pr\rho_r\beta_r T\overrightarrow{\boldsymbol{j}} + Ra_\Omega Pr\rho_r\beta_r Tsin(\Omega\tau)\overrightarrow{\boldsymbol{j}} \\ &= \rho_r\frac{\partial\overrightarrow{\boldsymbol{u}}}{\partial\tau} + \rho_r\overrightarrow{\boldsymbol{u}}.\nabla\overrightarrow{\boldsymbol{u}} \end{aligned} \tag{12}$$

The ratios appeared in the above equation, indicated by the subscript ***r***, are as follows:

$$\rho_r = \frac{\rho^*_{nl}}{\rho^*_{bl}}, \mu_r = \frac{\mu^*_{nl}}{\mu^*_{bl}}, \beta_r = \frac{\beta^*_{nl}}{\beta^*_{bl}} \tag{13}$$

In addition, the non-dimensional numbers corresponding to Prandtl (*Pr*), gravitational Rayleigh (Ra_g), and vibrational Rayleigh (Ra_Ω) are presented in Eq. (14).

$$Pr = \frac{\mu^*_{bl}}{\rho^*_{bl}\alpha^*_{bl}}, Ra_g = \frac{g^*\rho^*_{bl}\beta^*_{bl}\left(T^*_h - T^*_c\right)H^{*3}}{\mu^*_{bl}\alpha^*_{bl}}, Ra_\Omega = \frac{b^*\Omega^{*2}\rho^*_{bl}\beta^*_{bl}\left(T^*_h - T^*_c\right)H^{*3}}{\mu^*_{bl}\alpha^*_{bl}} \tag{14}$$

Additionally, the gravitational (non-vibrational), i.e., Gr_g, and vibrational Grashof, i.e., Gr_Ω, numbers are defined as:

$$Gr_g = \frac{Ra_g}{Pr} = \frac{g^*\beta^*_{bl}\left(T^*_h - T^*_c\right)H^{*3}}{\nu^{*2}_{bl}}, Gr_\Omega = \frac{b^*\Omega^{*2}\beta^*_{bl}\left(T^*_h - T^*_c\right)H^{*3}}{\nu^{*2}_{bl}} \tag{15}$$

where ν^*_{bl} is the kinematic viscosity of the base liquid. The enhancement ratio is calculated by comparing the Grashof number under vibrational conditions to the Grashof number without vibration. The formula for the enhancement ratio (*ER*) is expressed as:

$$ER = \frac{Gr_\Omega}{Gr_g} = \frac{b^*\Omega^{*2}}{g^*} \tag{16}$$

This ratio helps assess the impact of mechanical vibration on the convective heat transfer in a system. A higher enhancement ratio indicates that vibrational effects play a more significant role in heat transfer compared to non-vibrational conditions.

$$k_r\nabla^2 T = Cr\frac{\partial T}{\partial\tau} + Cr\overrightarrow{\boldsymbol{u}}.\nabla T \tag{17}$$

k_r is the ratio of the thermal conductivity of the nanoliquid to the base liquid. *Cr* of the above equations is:

$$Cr = \frac{\rho^*_{nl}C^*_{p,nl}}{\rho^*_{bl}C^*_{p,bl}} = 1 - \phi\left(1 - \varepsilon - T^{-1}_{Mr}Ste^{-1}f\right) \tag{18-a}$$

$$\varepsilon = \left[\rho^*_s\rho^*_{bl}C^*_{p,bl} + \zeta\rho^*_c\rho^*_{bl}C^*_{p,bl}\right]^{-1}\left[\rho^*_c\rho^*_s C^*_{p,c} + \zeta\rho^*_c\rho^*_s C^*_{p,s}\right] \tag{18-b}$$

$$T_{Mr} = T^*_{Mr}\left[T^*_h - T^*_c\right]^{-1}, Ste = \frac{\rho^*_{bl}C^*_{p,bl}\left(T^*_h - T^*_c\right)\left(\rho^*_s + \zeta\rho^*_c\right)}{L^*_{sf}\rho^*_c\rho^*_s} \tag{18-c}$$

It is worth emphasizing that *Cr*, designated as the heat capacity ratio, represents the ratio of the combined heat capacity (including latent and sensible heat capacities) of the nanoliquid to the sensible heat capacity of the base liquid. ε is the ratio of the heat capacity of the NEPCM particles to the base liquid. T_{Mr} is the non-dimensional melting temperature window, and *Ste* is the Stefan number. The non-dimensionalized function of *f* in *Cr* is:

$$f = \frac{\pi}{2} sin\left(\frac{\pi}{T_{Mr}}(T - T_m + T_{Mr}/2)\right)\sigma \tag{19-a}$$

$$\begin{cases} for\ T < (-T_{Mr}/2) + T_m \Rightarrow \sigma = 0 \\ for - (T_{Mr}/2) + T_m < T < (T_{Mr}/2) + T_m \Rightarrow \sigma = 1 \\ for\ T > (T_{Mr}/2) + T_m \Rightarrow \sigma = 0 \end{cases} \tag{19-b}$$

In extensive benchmark studies conducted by Buongiorno [37] and Venerus et al. [38], the impact of dispersing nano-sized particles on the viscosity and thermal conductivity of nanoliquids was examined. Numerous researchers from various regions worldwide have examined the properties mentioned above in nanofluids using diverse experimental setups and a range of measurement devices. The results indicate that it is feasible to express the thermal conductivity and viscosity of liquids incorporating nanoparticles through linear correlations. Building upon these findings, Ghalambaz et al. [39] used the derived linear correlations to investigate the characteristics of mass and heat transfer in nanoliquids:

$$k_r = \frac{k^*_{nl}}{k^*_{bl}} = \phi \times Nc + 1 \tag{20-a}$$

$$\mu_r = \frac{\mu^*_{nl}}{\mu^*_{bl}} = \phi \times Nv + 1 \tag{20-b}$$

In this context, *Nc* and *Nv* represent the numbers of the thermal conductivity and viscosity. The values of *Nc* and *Nv* are influenced by various factors, such as particle shape, the material of the nanoparticles, working temperature, and properties of the host liquid [39]. As evident from Eqs. (20), an elevation in the values of *Nv* and *Nc* leads to a more pronounced increase in the viscosity and thermal conductivity, respectively. By employing curve fitting on the collected empirical findings pertaining to the thermo-physical characteristics of suspensions, it is possible to determine *Nc* and *Nv*. The evaluation and reporting of a range of *Nc* and *Nv* values can be found in [39]. It is worth mentioning that these correlations are applicable specifically to diluted suspensions of nano-sized particles. For higher volume fractions of nano-sized particles, it is recommended to employ more advanced relations or rely on actual experimental data. In this study, the buoyancy ratio, represented as $\phi \times (\beta^*_{na}/\beta^*_{bl})$, is assumed to be negligible due to the small concentration of nano-sized particles, and the significantly lower thermal expansion of the NEPCM particles in comparison to the fluid phase.

The normalized boundary conditions are presented as the following:

$$for \begin{cases} x = 0 \\ 0 \le y \le 1 \end{cases} \Rightarrow \vec{\boldsymbol{u}} = 0, T = 1 \tag{21-a}$$

$$for \begin{cases} x = 1 \\ 0 \le y \le 1 \end{cases} \Rightarrow \vec{\boldsymbol{u}} = 0, T = 0 \tag{21-b}$$

$$for \begin{cases} y = 0 \\ y = 1 \\ 0 \le x \le 1 \end{cases} \Rightarrow \vec{\boldsymbol{u}} = 0, \frac{\partial T}{\partial y} = 0 \tag{21-c}$$

Finally, the dimensionless initial condition is:

$$for \begin{cases} 0 < x < 1 \\ 0 < y < 1 \\ t = 0 \end{cases} \Rightarrow \vec{\boldsymbol{u}} = \vec{\boldsymbol{u}}_{steady}, T = T_{steady} \tag{21-d}$$

The local Nusselt number at the hot surface is determined by employing the provided relation below:

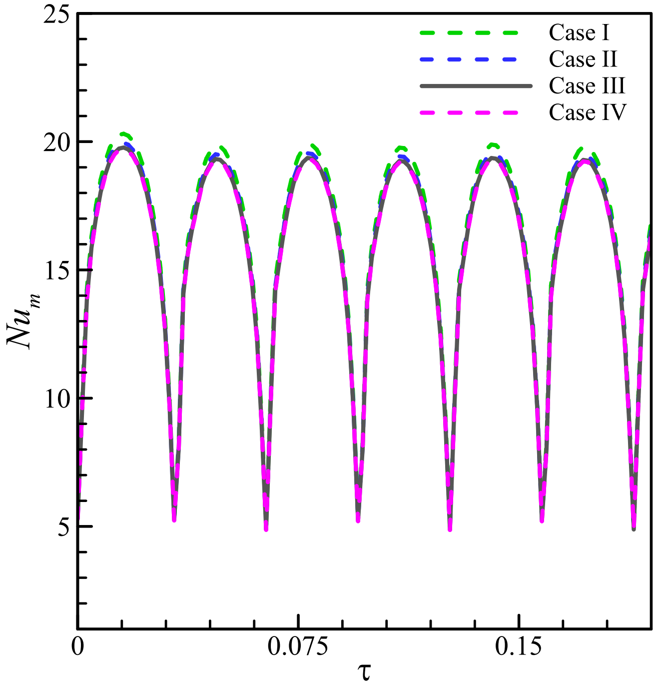

Fig. 2. The variations of Nu_m on the hot wall versus the non-dimensional time for different cases of grids at $Ra_g = 10^5$, $Ra_\Omega = 10^7$, $\Omega = 2\pi\xi = 100$, and $Pr = 0.71$.

$$Nu_l = -\frac{k^*_{nl}}{k^*_{bl}}\left(\frac{\partial T}{\partial x}\right)|_{hot\ wall} \tag{22}$$

Through the integration of the aforementioned equation along the hot surface, the time-dependent mean Nusselt number is derived:

$$Nu_m = \int_0^1 Nu_l\, dy \tag{23}$$

Ultimately, the time-averaged Nusselt number is:

$$Nu_{t,a} = \frac{\int_0^{\tau_{\max}} Nu_m\, d\tau}{\tau_{\max}} \tag{24}$$

5. Numerical approach, grid test, and validation

Analytical methods are impractical for solving the partial differential equations (PDEs) in the vast array of geometries that they encompass. Alternatively, a development of the PDEs approximation can be achieved, typically through various forms of discretizations. These discretization techniques create numerical model equations that serve as approximations for the PDEs. Employing numerical methods, these model equations can be solved, providing an estimate of the actual solution to the underlying PDEs. In this work, such approximations are calculated using the finite element method (FEM) [40]. In particular, we applied the Galerkin FEM to proficiently solve the governing Eqs. [41]. This approach involves initially partitioning the desired domain into smaller segments, followed by the formulation of a piecewise polynomial approximation for the solution within each of these segmented domains. Applying the Galerkin approach results in a system of algebraic equations solvable using conventional numerical methods [42]. To address the residual equations, we employ the PARallel DIrect SOlver, incorporating a Newtonian damping factor of 0.8 [43,44]. Iterations continue until the residual error criterion of 10^{-5} is met.

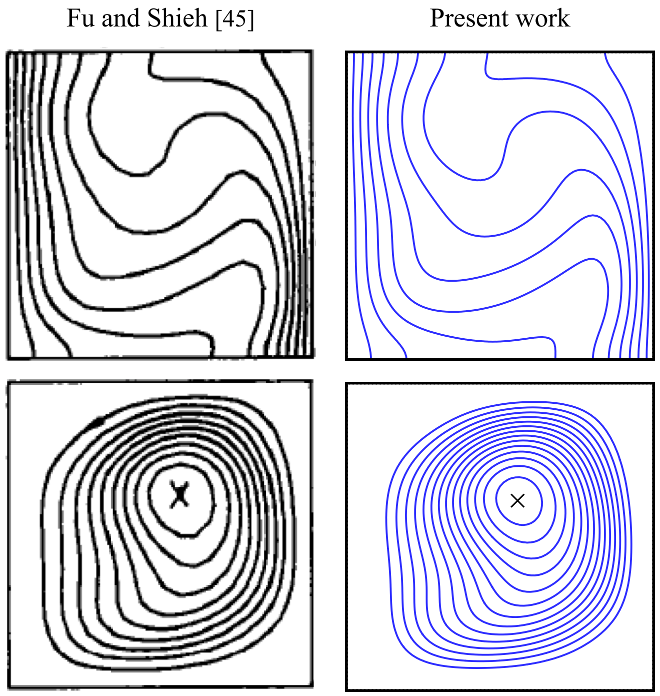

Fig. 3. Comparison between the isotherms and streamlines published in [45] and those derived in the current work for $Ra_g = 10^4$, $Ra_\Omega = 1.41 \times 10^5$, $\Omega = 2\pi\xi = 100$, $Pr = 0.71$.

The efficiency and accuracy of numerical computations directly depend on the size of the grids used. Consequently, it becomes imperative to perform a grid independence assessment in the current numerical analysis. This ensures the computational efficiency of simulations and aids in the selection of an optimal grid quantity. The numerical domain is meshed using control elements that are uniformly structured and quadrilateral. The grid independence test involves four distinct grid sizes. As shown in Fig. 2, with an increase in the grid number from 150 × 150 to 175 × 175, the variations in Nu_m are not visible. Consequently, a grid size consisting of 150 × 150 elements is opted for exploring the enclosure's performance under vibration.

To instill a high level of confidence in the outcomes of the ongoing work, validation studies are conducted, referencing the published papers in the literature [45,46]. The first work delves into the dynamics of a square cavity under vibration. Fig. 3 compares the isotherms and streamlines presented in [45] and those derived in the current work. The validation demonstrates an excellent alignment between the streamlines and isothermal contours, displaying a highly favorable matching behavior. Furthermore, the present work assesses the average Nusselt numbers on the hot wall at various time points by referencing the findings reported by Fu and Shieh [45]. The results, along with their corresponding errors tabulated in Table 1, demonstrate the high accuracy of results in the current study. Furthermore, to validate the algorithm for phase change and heat transfer of NEPCM-fluid mixture, we compare the average Nusselt number obtained in the current study with that presented in [46] for various parameters. Table 2 illustrates this assessment. As observed, the outcomes anticipated in this study closely align with the findings outlined in [46].

6. Simulation results

In this study, we evaluate the impacts of the gravitational Rayleigh number ($Ra_g = 10^2 - 10^5$), vibrational Rayleigh number ($Ra_\Omega = 10^3 - 10^7$), vibration frequency ($\xi = 4 - 20$), Stefan number ($Ste = 0.2 - 0.8$), melting temperature ($T_m = 0.1 - 0.9$), volume fraction of the NEPCM particles ($\phi = 0.0 - 0.05$), thermal conductivity number ($Nc = 0.0 - 6$), and dynamic viscosity number ($Nv = 0.0 - 6$) on the flow patterns and heat transfer rate. Here, the Prandtl number, i.e., Pr, is held constant at 6.2. Moreover, it is worth noting that the default values of the parameters are $Ra_g = 10^5$, $Ra_\Omega = 10^5$, $\xi = 16$, $Ste = 0.2$, $T_m = 0.25$, $\phi = 0.05$, and $Nc = Nv = 3$.

6.1. *Exploring the influence of vibrational Rayleigh number on governing fields: Streamlines, isotherms, and Cr contours*

Figs. 4 and 5 illustrate, respectively, the streamlines and isothermal contours within the cavity throughout a full oscillation cycle for different values of the vibrational Rayleigh number, Ra_Ω. Initially, it is observed that the patterns undergo disruption throughout the cycle, with the disturbance becoming more pronounced at higher values of Ra_Ω. For instance, for the lowest value of $Ra_\Omega = 10^3$, almost no change is found in the flow and thermal patterns. In this case, the enhancement ratio of Grashof number, i.e., ER, is 0.01. Here, the configuration is equivalent to the simple case of an enclosure with differential heating at its sides. The flow is composed of a single clockwise recirculation zone, corresponding to the convective flow. The heated fluid on the left ascends, driven by the buoyancy impacts, and is replaced by the inflowing colder nanoliquid from the right side. The isotherms are vertical and condensed near the active walls, indicating the dominance of conductive heat transfer in those zones. In contrast, they adopt a horizontal orientation in the middle, indicative of heat transport primarily through convection. When Ra_Ω is increased above 10^3, it starts to have an effect on the streamlines. Comparing the cases of $Ra_\Omega = 10^5$ to $Ra_\Omega = 10^7$, which the ER increases from 1.0 to 100, for $\Omega\tau = 2n\pi + \pi/2$, elevating Ra_Ω amplifies the intensity of the clockwise flow. Specifically, at this designated time, Ra_Ω aligns with Ra_g, reinforcing the convective flow in the same direction. At $\Omega\tau = 2n\pi + 3\pi/2$, the vibration effect opposes gravity, resulting in a reduction in the intensity of clockwise flow circulation as Ra_Ω increases. This trend continues until it eventually becomes counterclockwise at $Ra_\Omega = 10^7$ or $ER = 100$. In fact, as can be deduced from eq. (12), when $sin(\Omega\tau)$ is negative, the time-varying component of buoyancy force leads to the opposite impact of natural

Table 2
Average Nusselt number presented in [46] and those derived in the present work at different values of parameters for $Ra_g = 10^5$, $T_{Mr} = 0.05$, and $Pr = 6.2$.

Ste	T_m	ε	ρ^*_{na}/ρ^*_{bl}	Nc	Nv	Literature [46]	Present work
0.313	0.3	0.4	0.9	3.0	3.0	5.1932	5.1917
0.313	0.3	0.4	0.9	3.0	6.0	5.0030	5.0012
0.313	0.3	0.4	0.9	6.0	3.0	5.6533	5.6521
0.313	0.3	0.4	0.9	6.0	6.0	5.4477	5.4443
0.313	0.3	0.4	0.7	3.0	3.0	5.1933	5.1920
0.313	0.3	0.3	0.9	3.0	3.0	5.1864	5.1843
0.313	0.2	0.4	0.9	3.0	3.0	5.1022	5.1007
0.313	0.1	0.4	0.9	3.0	3.0	4.9550	4.9533
0.2	0.3	0.4	0.9	3.0	3.0	5.3541	5.3512

Table 1
Average Nusselt number presented in [45] and those derived in the present work at different times for $Ra_g = 10^4$, $Ra_\Omega = 1.41 \times 10^5$, $\Omega = 2\pi\xi = 100$, and $Pr = 0.71$.

τ	0.0120	0.0257	0.0361	0.0425	0.0500	0.0580	0.0899	0.1277
Fu and Shieh [45]	7.75	7.94	5.41	4.31	5.8	5.01	4.68	3.18
Present work	7.723	7.909	5.402	4.301	5.798	4.989	4.676	3.172
Error (%)	0.3484	0.3904	0.1479	0.2088	0.0345	0.4192	0.0855	0.2516

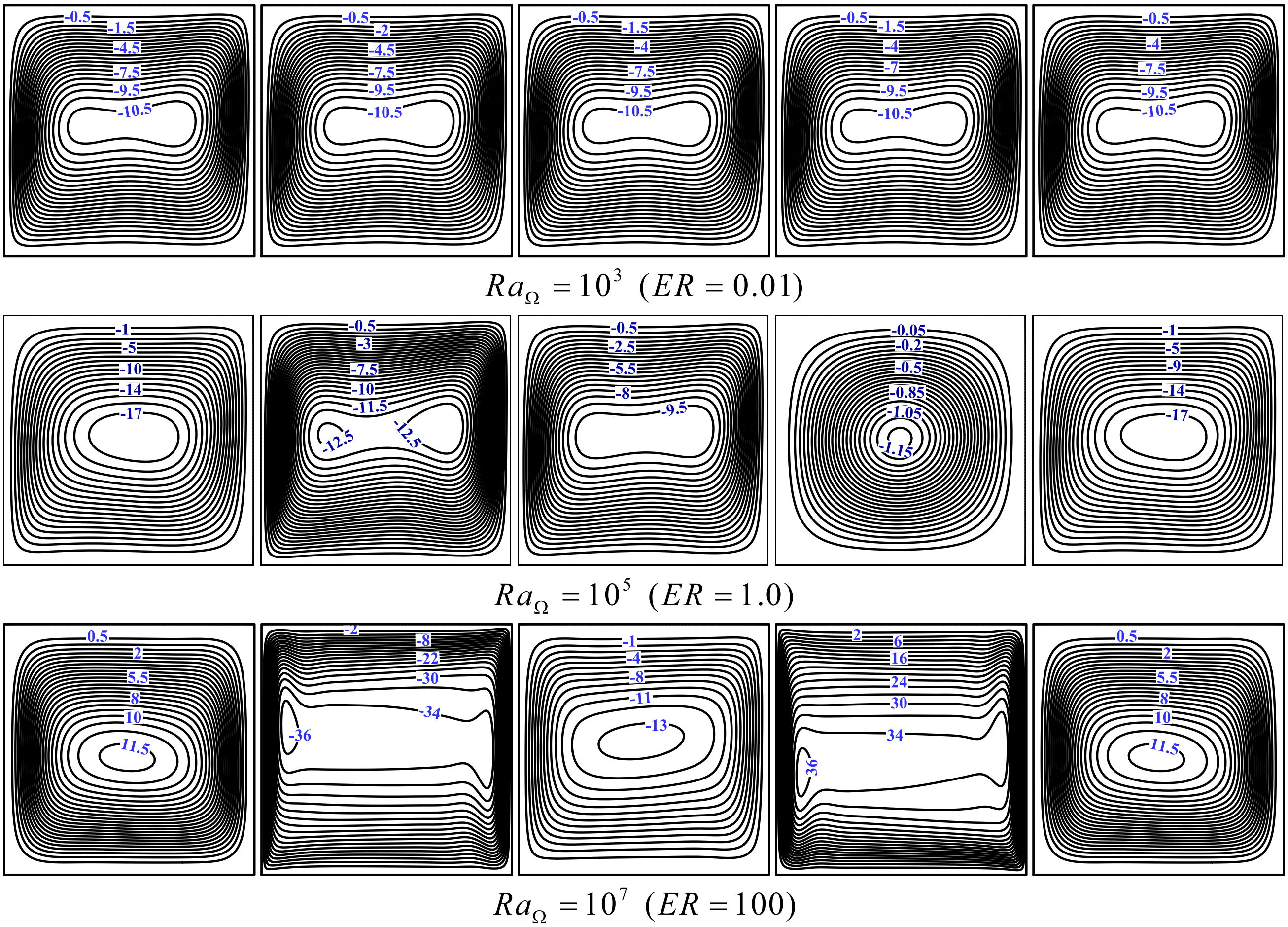

Fig. 4. Streamlines during one full cycle of oscillation for different values of vibrational Rayleigh number.

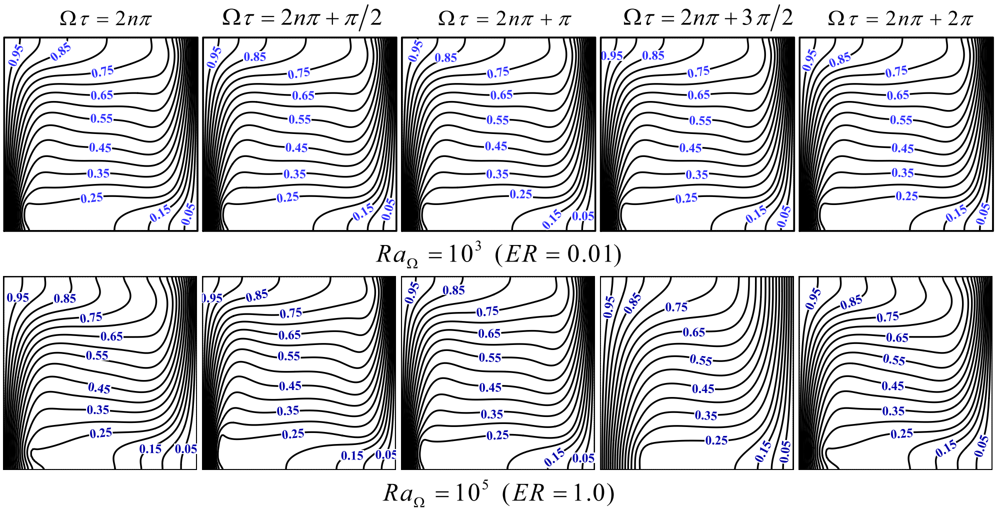

Fig. 5. Isotherms during one full cycle of oscillation for different values of vibrational Rayleigh number.

convection, such that the colder fluid ascends while the hotter one descends. For $Ra_{\Omega} = 10^7$, this component overcomes the gravity-induced convection, resulting in an adverse aspect of circulation. This can be further confirmed by looking at isotherms. It is seen that for all values of Ra_{Ω}, when $\Omega\tau = 2n\pi + \pi/2$, the colder isotherms, corresponding to temperatures like 0.05 and 0.15, occupy the bottom and right regions of the cavity, which is typical for free convective flows. On the other hand, when $\Omega\tau = 2n\pi + 3\pi/2$, the cold isotherms keep occupying the same regions for low Ra_{Ω} but exhibit a completely different behavior for higher Ra_{Ω}. For instance, for 10^7, cold isotherms extend upwards while hot ones move downwards, indicating that vibration-dominated convection acts opposite to free buoyancy-driven convection. The cases corresponding to $\Omega\tau = 2n\pi$, $\Omega\tau = 2n\pi + \pi$, and $\Omega\tau = 2n\pi + 2\pi$ are intermediate cases in which the time-varying term in buoyancy force is

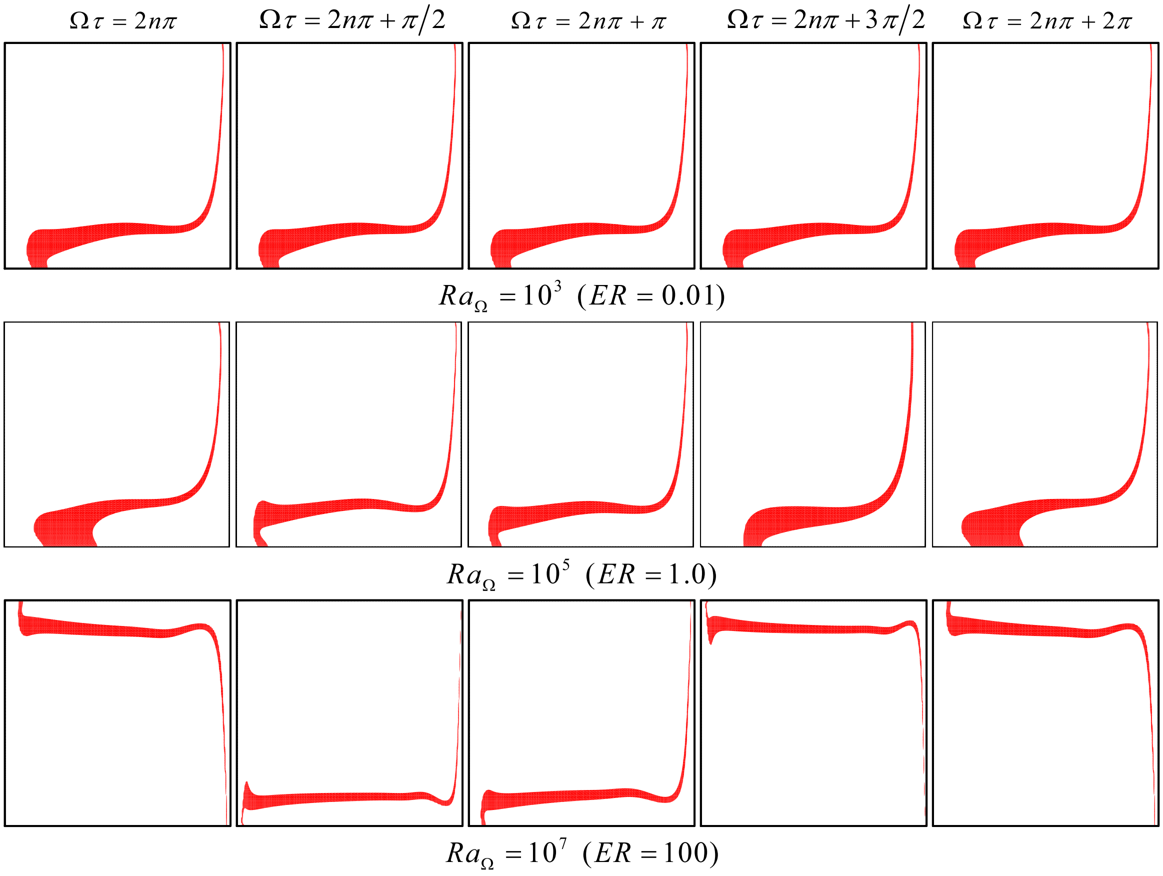

Fig. 6. *Cr* contours during one full cycle of oscillation for different values of vibrational Rayleigh number.

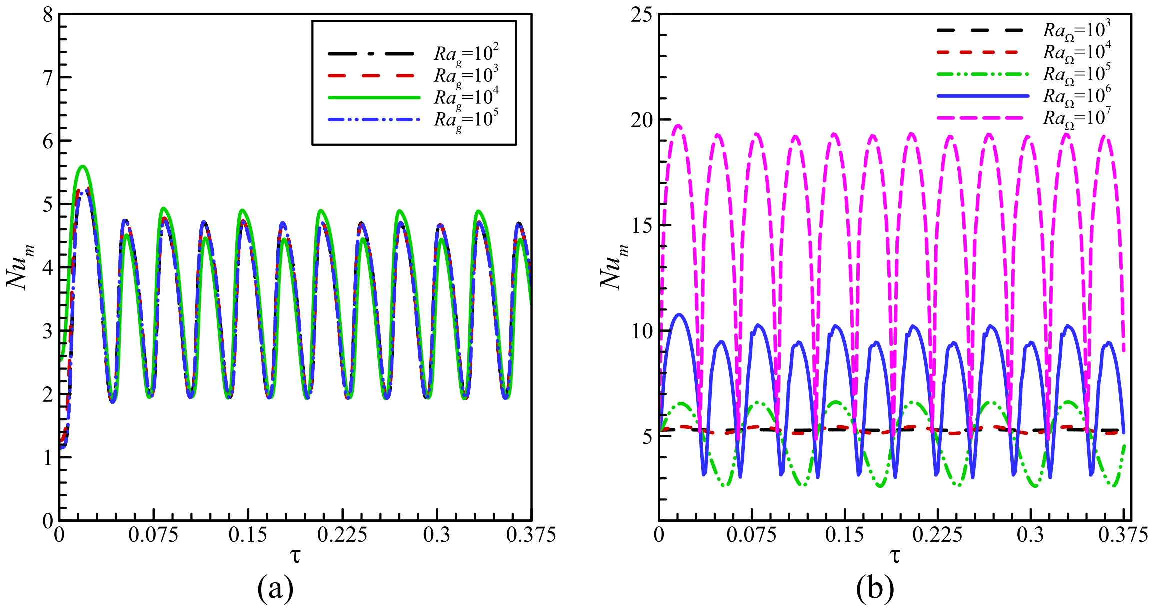

Fig. 7. Variations of Nu_m over time for various values of (a) Ra_g, ($Ra_g = 10^2$: $Nu_{t,a} = 3.4509$, $Ra_g = 10^3$: $Nu_{t,a} = 3.4520$, $Ra_g = 10^4$: $Nu_{t,a} = 3.4548$, $Ra_g = 10^5$: $Nu_{t,a} = 4.9203$) and (b) Ra_Ω, ($Ra_\Omega = 10^3$: $Nu_{t,a} = 5.2906$, $Ra_\Omega = 10^4$: $Nu_{t,a} = 5.2905$, $Ra_\Omega = 10^5$: $Nu_{t,a} = 4.9203$, $Ra_\Omega = 10^6$: $Nu_{t,a} = 7.5420$, $Ra_\Omega = 10^7$: $Nu_{t,a} = 15.735$).

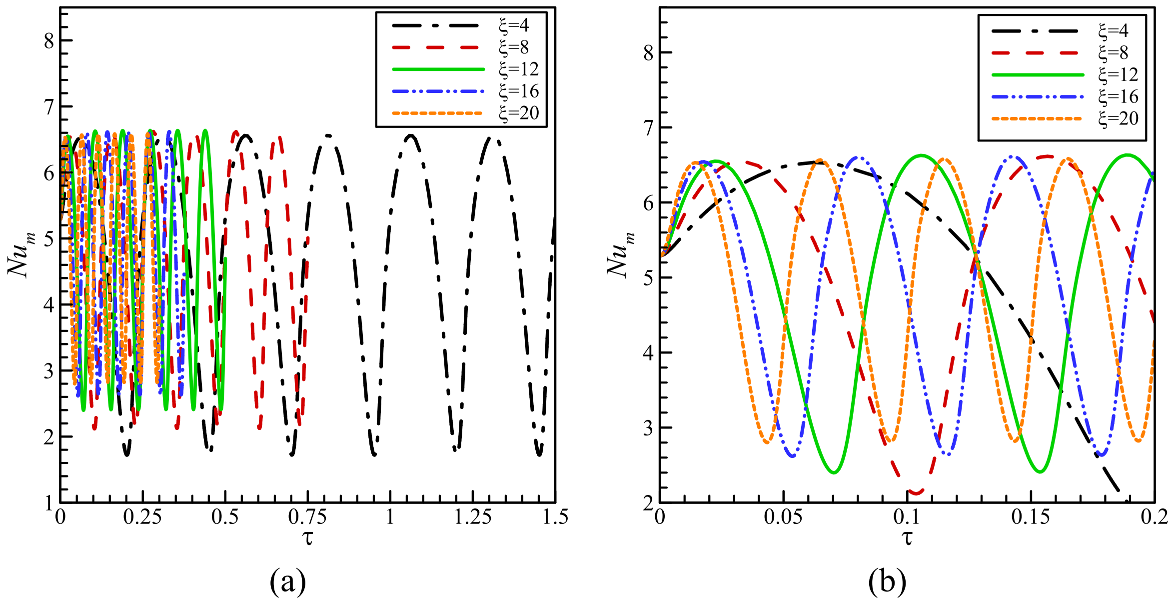

Fig. 8. Variations of Nu_m on the heated surface over time for various values of frequency during (a) full computational time, and (b) $0.0 \leq \tau \leq 0.2$. $\xi = 4$ ($Nu_{t,a} = 4.8003$), $\xi = 8$ ($Nu_{t,a} = 4.8471$), $\xi = 12$ ($Nu_{t,a} = 4.8848$), $\xi = 16$ ($Nu_{t,a} = 4.9203$), and $\xi = 20$ ($Nu_{t,a} = 4.9504$).

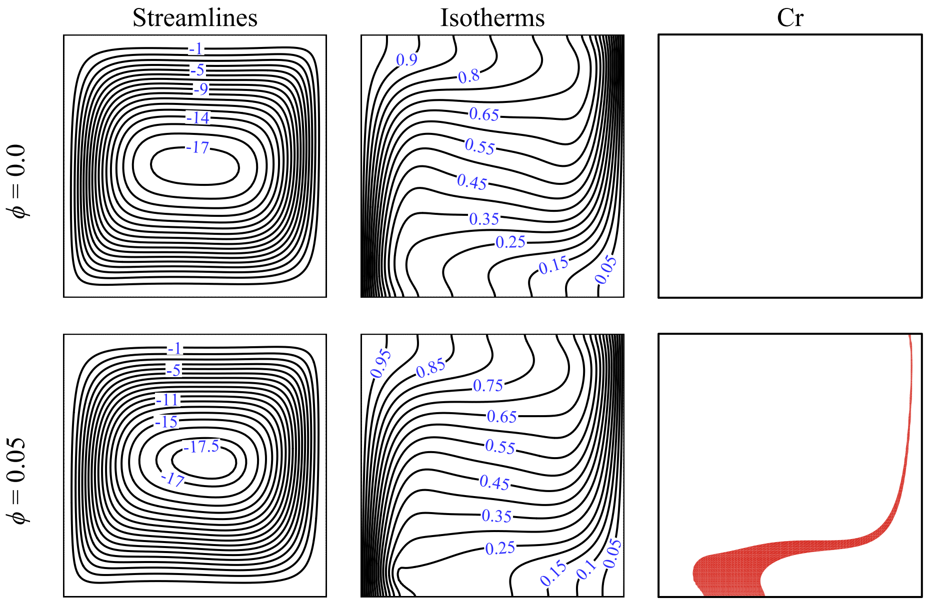

Fig. 9. Streamlines, isotherms, and Cr contours at $\phi = 0.0$ and $\phi = 0.05$.

momentarily zero, and its value changes its sign from positive to negative and vice versa. For this reason, the behavior of fluid at these instants depends on its previous state. The two cases of $\Omega\tau = 2n\pi$ and $\Omega\tau = 2n\pi + 2\pi$ present the same patterns, as the fluid completes a full oscillation cycle and start a new one.

Fig. 6 depicts contours of the specific heat ratio, i.e., Cr, during an oscillation cycle for various values of Ra_Ω. It should be noted that the red zones in the cavity correspond to the area where the core of the NEPCM particles undergoes phase change. As can be seen, the melting zones follow the isotherm corresponding to the melting temperature of the PCM, which is $T_m = 0.25$. For low Ra_Ω, NEPCM particles undergoes melting in the bottom region of the enclosure. But when Ra_Ω is increased above 10^5, the location of the melting shifts from downwards to upwards when the convective flow is enhanced by the vibration, as discussed previously about the isotherms in Fig. 5.

6.2. Influence of the vibration frequency and vibrational Rayleigh number on heat transfer rate (time-dependent mean Nusselt number and time-averaged Nusselt number)

The variations in the average Nusselt number, i.e., Nu_m, over time for various gravitational and vibrational Rayleigh numbers, Ra_g and Ra_Ω, are plotted in Fig. 7. The variation of Nu_m oscillates in all the cases, following the fluid's vibration. It is clear that Ra_g has a slight effect on the variation of Nu_m while the vibration dominates the flow and thermal behaviors. On the other hand, Ra_Ω has a substantial effect on Nu_m, whose amplitude increases for higher Ra_Ω. Indeed, since heat transfer is predominantly governed by vibration-induced convection, it is intensified when the vibration effect is stronger, i.e., for high values of Ra_Ω or ER. In addition, more mixing between the hot and cold regions of the fluid occurs for high Ra_Ω, as the location of the cold and hot fluid keeps

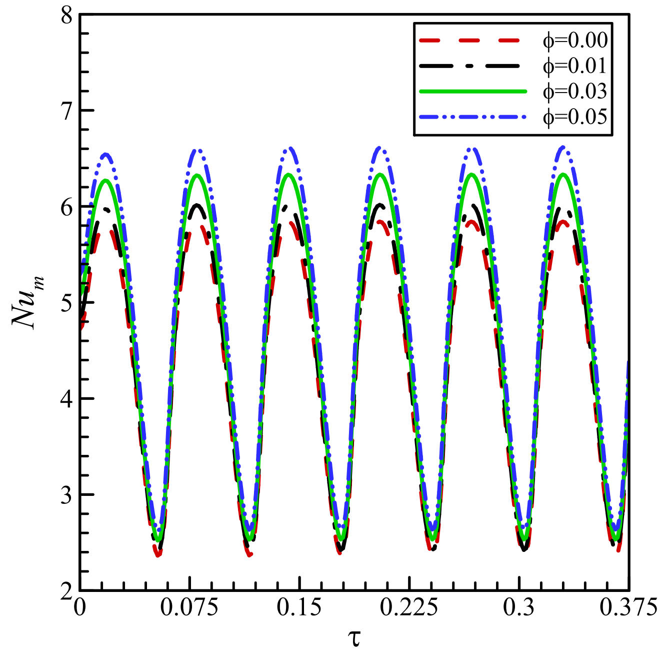

Fig. 10. Variations of Nu_m over time for various values of ϕ; $\phi = 0.0$ ($Nu_{t,a} = 4.3872$), $\phi = 0.01$ ($Nu_{t,a} = 4.5028$), $\phi = 0.03$ ($Nu_{t,a} = 4.7197$), and $\phi = 0.05$ ($Nu_{t,a} = 4.9203$).

shifting with the oscillation, as previously discussed, leading to an enhanced heat transfer. Namely, a 300% increase in the time-averaged heat transfer is obtained when Ra_Ω is raised from 10^3 to 10^7 (or *ER* increase from 0.01 to 100).

Fig. 8(a) and (b) show the temporal evolution of Nu_m for various values of the ordinary frequency of oscillation, i.e., ξ. A focus on the time interval $0.0 \le \tau \le 0.2$ is shown in Fig. 8(b). The frequency only affects the number of oscillations per time unit, with a very slight impact on the intensity of heat transfer. The amplitude of Nu_m remains almost the same for all considered values of ξ. Only a 3% change in the time-averaged Nusselt number is observed when ξ is raised from 4 to 20. This is because the vibration-induced convection, expressed by Ra_Ω, is related to the amplitude of the oscillation rather than its frequency.

6.3. Impact of volume fraction of NEPCM particles on the governing fields and heat transfer rate

A comparison of the streamlines, isotherms, and *Cr* contours for cases involving a pure fluid and a nanofluid with a concentration of 0.05 of the NEPCM particles is presented in Fig. 9. As can be seen, the nanoparticles have a negligible effect on the flow patterns, given that the small particle concentration used is insufficient to disturb the flow circulation. Additionally, the impact of nanoparticles on the flow patterns is localized at the bottom, in the vicinity of the isotherm corresponding to the dimensionless temperature 0.25, which represents the melting temperature of the NEPCM particles core. In that location, the melting of the PCM absorbs part of the heat and delays the development of the thermal gradient away from the heated wall. This is evident in the isotherm 0.25, which extends toward the heated wall in the presence of the nano-sized particles. This observation can be further illustrated in Fig. 10, as there is a subtle rise in the amplitude of Nu_m with the increase in ϕ. Namely, a 12% increase in the time-averaged Nusselt number is reached when nanoparticles with a concentration of 5% are dispersed in the fluid instead of a pure fluid.

Table 3
Time-averaged Nusselt number for different values of Stefan number.

Ste	0.2	0.4	0.6	0.8
$Nu_{t,a}$	4.9203	4.7258	4.6551	4.6183

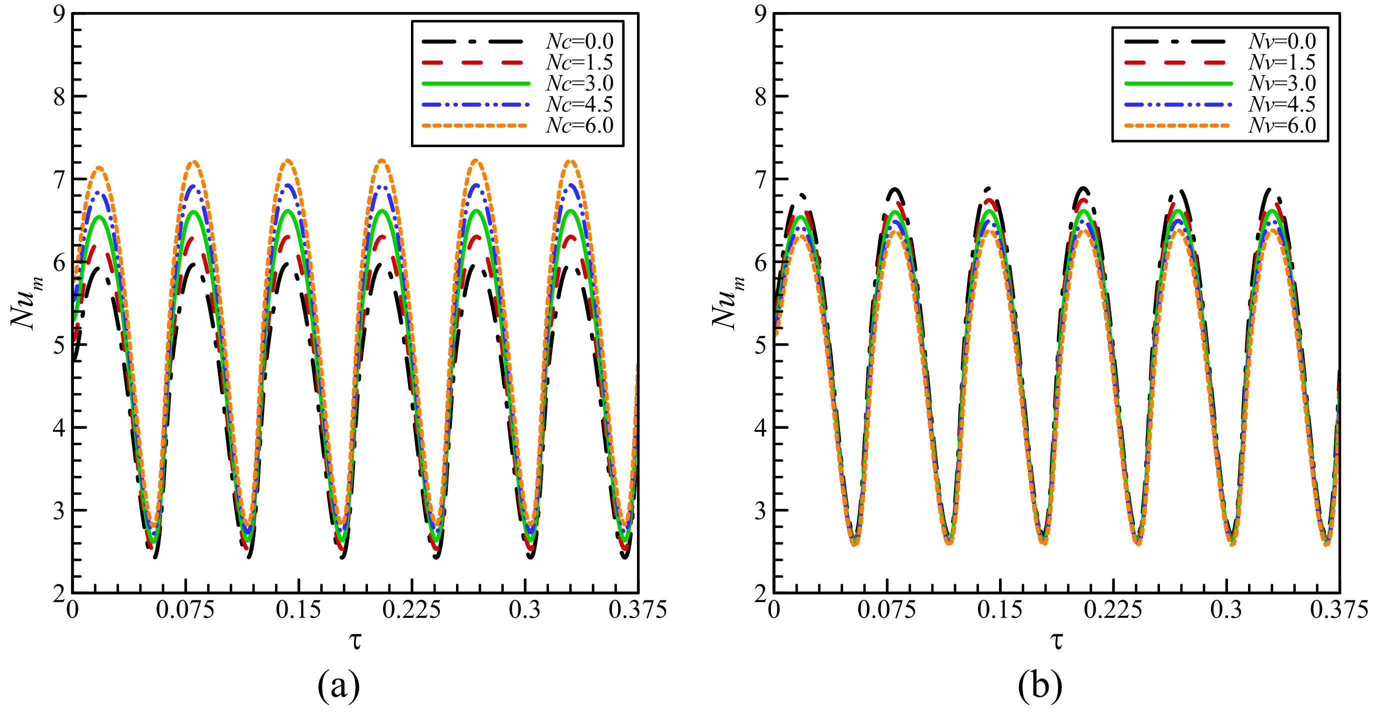

(a)

(b)

Fig. 11. Variations of Nu_m over time for various values of (a) *Nc*; ($Nc = 0.0$: $Nu_{t,a} = 4.4697$, $Nc = 1.5$: $Nu_{t,a} = 4.6981$, $Nc = 3.0$: $Nu_{t,a} = 4.9203$, $Nc = 4.5$: $Nu_{t,a} = 5.1385$, $Nc = 6.0$: $Nu_{t,a} = 5.3512$), and (b) *Nv*; ($Nv = 0.0$: $Nu_{t,a} = 5.1224$, $Nv = 1.5$: $Nu_{t,a} = 5.0181$, $Nv = 3.0$: $Nu_{t,a} = 4.9203$, $Nv = 4.5$: $Nu_{t,a} = 4.8307$, $Nv = 6.0$: $Nu_{t,a} = 4.7463$).

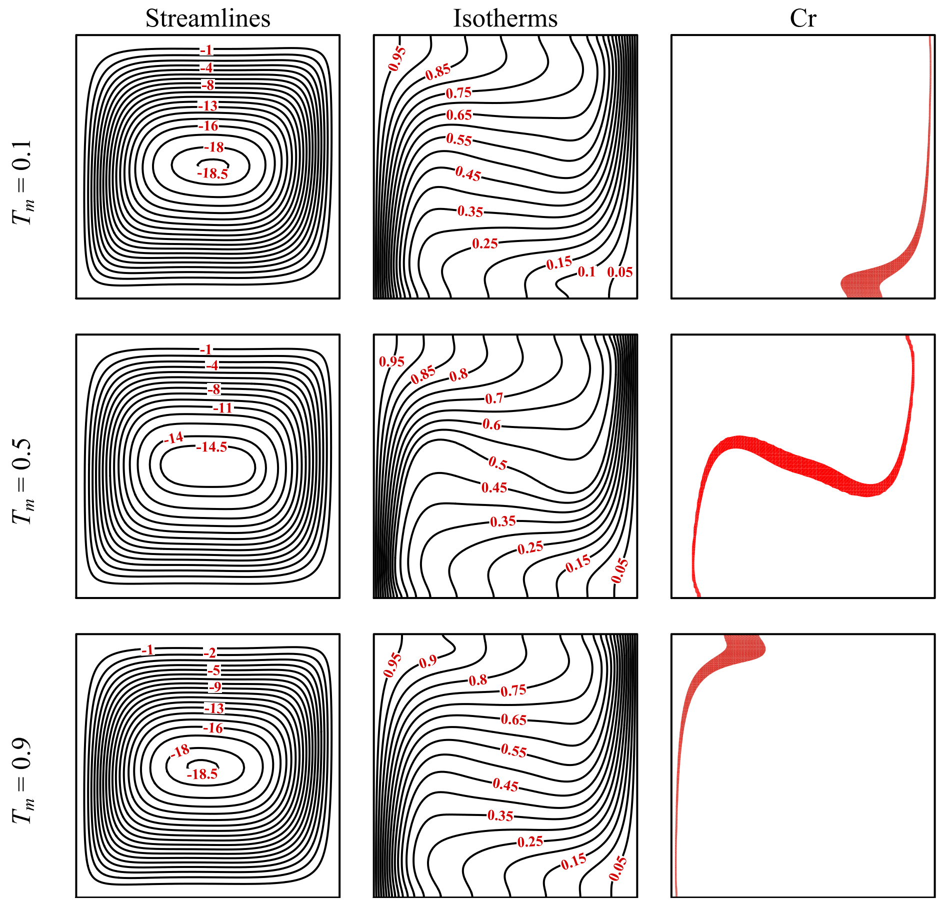

Fig. 12. Streamlines, isotherms, and *Cr* ratio at different values of melting temperature (T_m).

Table 4
Time-averaged Nusselt number for different values of melting temperature.

T_m	0.1	0.25	0.5	0.75	0.9
$Nu_{t,a}$	4.6356	4.9203	4.9540	4.9299	4.6383

6.4. Impact of Nc, Nv, and Ste on the heat transfer rate

The effect of thermal conductivity and viscosity numbers on the time variation of Nu_m is shown in Figs. 11(a) and (b), respectively. Higher values of *Nc* lead to a rise in Nu_m, while the opposite is found in the case of *Nv*. In fact, raising *Nc* indicates a higher thermal conductivity of the nanoliquid, which enhances the heat transmission through the fluid. Conversely, increasing *Nv* expresses a rise in the viscosity of the fluid, resulting to hindered flow circulation and diminished the convective heat transfer in the enclosure. Overall, a 26% increase and a 7.3% reduction in the time-average heat transfer are observed when *Nc* and *Nv*, respectively, are raised from 0 to 6.

The time-averaged Nusselt numbers for different values of *Ste* are presented in Table 3. A 6.1% rise in the time-averaged Nusselt number is obtained when *Ste* is reduced from 0.8 to 0.2. This relationship arises from the inverse correlation between the Stefan number and the latent heat of the nano-sized particles. A decrease in the Stefan number corresponds to an increase in the involvement of the core of nano-sized particles in the overall process of heat transfer.

6.5. Impact of the melting temperature of nanoparticles core on the governing fields and heat transfer rate

Flow patterns, contours of temperature, and *Cr* are illustrated in Fig. 12 for different values of the melting temperature of the NEPCM particles core, i.e., T_m. Naturally, the main impact of T_m is on the *Cr* contours, as PCM melts when the temperature in vicinity of the PCM is equal to T_m. For this reason, changing T_m from 0.1 to 0.9 changes the PCM melting zone from being localized at the bottom right of the cavity to its upper left corner. When T_m is 0.5, the melting of the PCM extends from the bottom left through the middle of the cavity to the upper right side, influenced by the temperature distribution between the heated and cooled walls. The influence of PCM melting on temperature contours is particularly concentrated on the isotherms with temperatures close to T_m. The phase change occurs at a constant temperature, altering the extent of the isotherms in its vicinity.

The variations of time-averaged Nusselt number for different values of T_m are tabulated in Table 4. As seen, the maximum time-averaged Nusselt number occurs for $T_m = 0.5$, while the minimum is for $T_m =$ 0.1 and 0.9. In fact, in the latter cases, the melting of the PCM is confined to the vicinity of the active walls, as previously indicated. This limitation restricts the contribution of the PCM to the heat transfer, contrasting with the case $T_m = 0.5$, where the phase transition covers the middle of the chamber. In any case, the impact of the fusion temperature on the thermal behavior of the suspension remains limited, with only a 6.5% increase in the time-averaged heat transfer observed when T_m is raised from 0.1 to 0.5.

7. Summary and conclusion

The integrated effects of buoyancy and vibration on the thermal response and flow dynamic of an aqueous solution containing nano-encapsulated phase change material (NEPCM) particles were analyzed through numerical simulation. The aqueous solution was confined within a square enclosure with differential heating at its side walls. The gravity term in the momentum equation was modified to include the effect of sinusoidal vibration. The objective was to assess the influence of several parameters, namely the vibrational Rayleigh number Ra_Ω, gravitational Rayleigh number Ra_g, ordinary frequency ζ, particle concentration ϕ, conductivity and viscosity numbers Nc and Nv, Stefan number Ste, and melting temperature T_m on the streamlines, isotherms, and melting fields. Additionally, the impact of these parameters was investigated on the time variations of the mean Nusselt number, i.e., Nu_m, and the time-averaged heat transfer, i.e., $Nu_{t,a}$. The summary of the findings is presented as follows:

- The simulations reveal that Ra_Ω is the parameter with the most influence on the vibration-induced convection. Increasing Ra_Ω (or ER) from 10^3 (or 0.01) to 10^7 (or 100) triples the time-averaged Nusselt number in the cavity. However, the time-averaged Nusselt number increases by 42% as Ra_g varies from 10^2 to 10^5.
- The time-averaged Nusselt number experiences only 3.1% increase as the angular frequency, i.e., Ω, rises from 8π to 40π.
- Raising the conductivity of the nanoliquid through Nc and its viscosity via Nv leads to an improvement and hindrance of convective heat transfer. The effect of Nc is more pronounced, as increasing it from 0 to 6 can lead to up to 26% rise in the time-averaged heat transfer. Conversely, elevating the viscosity number, i.e., Nv, from 0 to 6 is associated with a 7.3% reduction in the time-averaged Nusselt number.
- The nanoparticle concentration has a positive impact on heat transfer rate, undergoing an augmentation of 12% when a nanoliquid with a 5% volume fraction is used instead of a pure liquid.
- The melting temperature and Stefan number has a relatively limited effect on heat transfer. When varying the melting temperature from 0.1 to 0.9, the maximum rate of heat transfer is observed at the melting temperature of 0.5, showing an approximate 6.5% difference compared to the melting temperatures of 0.1 and 0.9. Furthermore, increasing the Stefan number from 0.2 to 0.8 leads to an approximate 6.1% reduction in the time-averaged Nusselt number.

These results can improve our understanding of the various aspects affecting vibrational convection and the methods that can be employed to enhance thermal performance. This improvement can be achieved either by varying the mechanical vibration characteristics or through the use of enhanced liquid suspensions with the NEPCM particles.

CRediT authorship contribution statement

Nidhal Ben Khedher: Conceptualization, Formal analysis, Methodology, Software, Validation, Writing – original draft. **S.A.M. Mehryan:** Conceptualization, Formal analysis, Investigation, Methodology, Software, Supervision, Writing – original draft. **Ahmad Hajjar:** Data curation, Methodology, Resources, Visualization, Writing – original draft. **Abed Saif Alghawli:** Formal analysis, Project administration, Resources, Validation, Writing – review & editing. **Mohammad Ghalambaz:** Conceptualization, Formal analysis, Investigation, Software, Supervision, Validation. **Kasra Ayoubi Ayoubloo:** Investigation, Software, Visualization, Writing – review & editing. **Sami Dhahbi:** Data curation, Resources, Software, Writing – review & editing.

Declaration of Competing Interest

The authors declare that they have no conflict of interest.

Data availability

No data was used for the research described in the article.

Acknowledgments

The authors extend their appreciation to the Deanship of Scientific Research at King Khalid University for funding this work through large group Research Project under grant number RGP2/337/44.

References

[1] H. Zhu, Y. Lu, L. Cai, Wavelength-shift-free racetrack resonator hybrided with phase change material for photonic in-memory computing, Opt. Express 31 (12) (2023) 18840–18850, https://doi.org/10.1364/OE.489525.

[2] S. Yang, Y. Zhang, Z. Sha, Z. Huang, H. Wang, F. Wang, J. Li, Deterministic manipulation of heat flow via three-dimensional-printed thermal meta-materials for multiple protection of critical components, ACS Appl. Mater. Interfaces 14 (34) (2022) 39354–39363.

[3] L. Zhou, F. Meng, Y. Sun, Numerical study on infrared detectors cooling by multi-stage thermoelectric cooler combined with microchannel heat sink, Appl. Therm. Eng. 236 (2024) 121788, https://doi.org/10.1016/j.applthermaleng.2023.121788.

[4] X. Zhang, Y. Tang, F. Zhang, C.S. Lee, A novel aluminum–graphite dual-ion battery, Adv. Energy Mater. 6 (11) (2016) 1502588.

[5] F. Farzaneh, S. Jung, Experimental and numerical investigation on enhancing capped-end tube energy absorption capacity by orifice effect, Structures 53 (2023) 1450–1462, https://doi.org/10.1016/j.istruc.2023.05.015.

[6] E. Saedpanah, M. Lahonian, M.Z. Malek Abad, Optimization of multi-source renewable energy air conditioning systems using a combination of transient simulation, response surface method, and 3E lifespan analysis, Energy 272 (2023) 127200, https://doi.org/10.1016/j.energy.2023.127200.

[7] Y. Zhang, X. He, X. Cong, Q. Wang, H. Yi, S. Li, C. Zhang, T. Zhang, X. Wang, Q. Chi, Enhanced energy storage performance of polyethersulfone-based dielectric composite via regulating heat treatment and filling phase, J. Alloys Compd. 960 (2023) 170539, https://doi.org/10.1016/j.jallcom.2023.170539.

[8] Y. Lu, M. Stegmaier, P. Nukala, M.A. Giambra, S. Ferrari, A. Busacca, W.H. Pernice, R. Agarwal, Mixed-mode operation of hybrid phase-change nanophotonic circuits, Nano Lett. 17 (1) (2017) 150–155.

[9] S.A. Albdour, Z. Haddad, O.Z. Sharaf, A. Alazzam, E. Abu-Nada, Micro/nano-encapsulated phase-change materials (ePCMs) for solar photothermal absorption and storage: fundamentals, recent advances, and future directions, Prog. Energy Combust. Sci. 93 (2022) 101037.

[10] M.S. Ghoghaei, A. Mahmoudian, O. Mohammadi, M.B. Shafii, H. Jafari Mosleh, M. Zandieh, M.H. Ahmadi, A review on the applications of micro−/nano-encapsulated phase change material slurry in heat transfer and thermal storage systems, J. Therm. Anal. Calorim. 145 (2021) 245–268.

[11] C. Ho, Y.-C. Liu, T.-F. Yang, M. Ghalambaz, W.-M. Yan, Convective heat transfer of nano-encapsulated phase change material suspension in a divergent minichannel heatsink, Int. J. Heat Mass Transf. 165 (2021) 120717.

[12] W. Li, D. Zhang, T. Jing, M. Gao, P. Liu, G. He, F. Qin, Nano-encapsulated phase change material slurry (Nano-PCMS) saturated in metal foam: a new stable and efficient strategy for passive thermal management, Energy 165 (2018) 743–751.

[13] A. Sarı, C. Alkan, C. Bilgin, A. Bicer, Preparation, characterization and thermal energy storage properties of micro/nano encapsulated phase change material with acrylic-based polymer, Polym. Sci., Ser. B 60 (2018) 58–68.

[14] M. Hashemi-Tilehnoee, A. Dogonchi, S.M. Seyyedi, M. Sharifpur, Magneto-fluid dynamic and second law analysis in a hot porous cavity filled by nanofluid and nano-encapsulated phase change material suspension with different layout of cooling channels, J. Energy Stor. 31 (2020) 101720.

[15] Z. Raizah, A.M. Aly, Double-diffusive convection of a rotating circular cylinder in a porous cavity suspended by nano-encapsulated phase change materials, Case Stud. Thermal Eng. 24 (2021) 100864.

[16] A.M. Aly, E.M. Mohamed, M.F. El-Amin, N. Alsedais, Double-diffusive convection between two different phases in a porous infinite-shaped enclosure suspended by nano encapsulated phase change materials, Case Stud. Thermal Eng. 26 (2021) 101016.

[17] S. Hussain, N. Alsedias, A.M. Aly, Natural convection of a water-based suspension containing nano-encapsulated phase change material in a porous grooved cavity, J. Energy Stor. 51 (2022) 104589.

[18] Z. Raizah, A.M. Aly, A rotating superellipse inside a hexagonalshaped cavity suspended by nano-encapsulated phase change materials based on the ISPH method, Int. J. Num. Methods Heat Fluid Flow 32 (3) (2022) 956–977.

[19] A.M. Aly, A.K. Hussein, O. Younis, N. Alsedais, L. Kolsi, Double-diffusive convection of two rods in a novel cavity saturated by porous media and suspended by nano-encapsulated phase change materials, Waves Random Complex Media (2022) 1–25.

[20] S. Hussain, A.M. Aly, N. Alsedias, Bioconvection of oxytactic microorganisms with nano-encapsulated phase change materials in an omega-shaped porous enclosure, J. Energy Stor. 56 (2022) 105872.
[21] H. Kazemi-Varnamkhasti, I. Khazaee, M. Ameri, D. Toghraie, Heat storage and increasing the rate of heat transfer in polymer electrolyte membrane fuel cell by adding nano-encapsulated phase change material to water in the cooling process, J. Energy Stor. 59 (2023) 106497.
[22] S.E. Ahmed, Z.A. Raizah, Analysis of the entropy due to radiative flow of nano–encapsulated phase change materials within inclined porous prismatic enclosures: finite element simulation, J. Energy Stor. 40 (2021) 102719.
[23] A. Alazzam, N.A. Qasem, A. Aissa, M.S. Abid, K. Guedri, O. Younis, Natural convection characteristics of nano-encapsulated phase change materials in a rectangular wavy enclosure with heating element and under an external magnetic field, J. Energy Stor. 57 (2023) 106213.
[24] P. Wang, X. Wu, X. He, Vibration-theoretic approach to vulnerability analysis of nonlinear vehicle platoons, IEEE Trans. Intell. Transp. Syst. 24 (10) (2023) 11334–11344.
[25] Z.-Q. Lu, D. Wu, H. Ding, L.-Q. Chen, Vibration isolation and energy harvesting integrated in a Stewart platform with high static and low dynamic stiffness, Appl. Math. Model. 89 (2021) 249–267.
[26] N.K. Murad, H.D. Lafta, S. Elis Abdullah, The effect of transverse vibration on the natural convection heat transfer in a rectangular enclosure, Int. J. Mech. Eng. Technol. 10 (6) (2019).
[27] R.E. Forbes, C.T. Carley, C.J. Bell, Vibration Effects on Convective Heat Transfer in Enclosures, 1970.
[28] K.H. Kim, J.M. Hyun, H.S. Kwak, Buoyant convection in a side-heated cavity under gravity and oscillations, Int. J. Heat Mass Transf. 44 (4) (2001) 857–861.
[29] A. Purusothaman, A.J. Chamkha, Combined effects of mechanical vibration and magnetic field on the onset of buoyancy-driven convection in an anisotropic porous module, J. Porous Media 22 (11) (2019).
[30] A. Purusothaman, R.C.G. Sekar, K. Murugesan, Magnetic field and vibration effects on the onset of thermal convection in a grade fluid permeated anisotropic porous module, Thermal Sci. Eng. Prog. 10 (2019) 138–146.
[31] J.M. Jalil, K.A. Al-Tae'y, Thermovibrational convection in an enclosure with magnetic field damping, Num. Heat Transf. Part A: Appl. 53 (7) (2007) 766–786.
[32] M.C. Önen, M. Arici, Enhancing natural convection through mechanical vibration: Eccentric rotation of square cavity, in: ICTEA: International Conference on Thermal Engineering, 2023.
[33] M.C. Mojtabi, Y. Razi, K. Maliwan, A. Mojtabi, Effect of vibration on the onset of double-diffusive convection in porous media, in: Transport Phenomena in Porous Media III, Elsevier, 2005, pp. 261–286.
[34] E.-H. Zidi, A. Hasseine, N. Moummi, The effect of vertical vibrations on heat and mass transfers through natural convection in partially porous cavity, Arab. J. Sci. Eng. 43 (2018) 2195–2204.
[35] S. Mehryan, P. Goudarzi, S.M.H. Zadeh, M. Ghodrat, O. Younis, M. Ghalambaz, Thermal vibrational and gravitational analysis of a hybrid aqueous suspension comprising Ag–MgO hybrid nano-additives, Int. Commun. Heat Mass Transf. 126 (2021) 105345.
[36] M.J. Pour Razzaghi, M. Asadollahzadeh, M.R. Tajbakhsh, R. Mohammadzadeh, M. Zare Malek Abad, E. Nadimi, Investigation of a temperature-sensitive ferrofluid to predict heat transfer and irreversibilities in LS-3 solar collector under line dipole magnetic field and a rotary twisted tape, Int. J. Therm. Sci. 185 (2023) 108104, https://doi.org/10.1016/j.ijthermalsci.2022.108104.
[37] J. Buongiorno, D.C. Venerus, N. Prabhat, T. McKrell, J. Townsend, R. Christianson, Y.V. Tolmachev, P. Keblinski, L.-W. Hu, J.L. Alvarado, A benchmark study on the thermal conductivity of nanofluids, J. Appl. Phys. 106 (9) (2009).
[38] D.C. Venerus, J. Buongiorno, R. Christianson, J. Townsend, I.C. Bang, G. Chen, S. J. Chung, M. Chyu, H. Chen, Y. Ding, Viscosity measurements on colloidal dispersions (nanofluids) for heat transfer applications, Appl. Rheol. 20 (4) (2010) 44582.
[39] M. Ghalambaz, A. Doostani, E. Izadpanahi, A.J. Chamkha, Phase-change heat transfer in a cavity heated from below: the effect of utilizing single or hybrid nanoparticles as additives, J. Taiwan Inst. Chem. Eng. 72 (2017) 104–115, https://doi.org/10.1016/j.jtice.2017.01.010.
[40] J. Xu, L. Chang, T. Chen, T. Ren, Y. Zhang, Z. Cai, Study of the bending properties of variable stiffness chain mail fabrics, Compos. Struct. 322 (2023) 117369, https://doi.org/10.1016/j.compstruct.2023.117369.
[41] R.L. Taylor, O.C. Zienkiewicz, The Finite Element Method, Butterworth-Heinemann Oxford, 2013.
[42] Author biography, in: O.C. Zienkiewicz, R.L. Taylor, P. Nithiarasu (Eds.), The Finite Element Method for Fluid Dynamics, Seventh edition, Butterworth-Heinemann, Oxford, 2014, p. ii, https://doi.org/10.1016/B978-1-85617-635-4.00017-0.
[43] O. Schenk, K. Gärtner, Solving unsymmetric sparse systems of linear equations with PARDISO, Futur. Gener. Comput. Syst. 20 (3) (2004) 475–487.
[44] P. Wriggers, Nonlinear Finite Element Methods, Springer Science & Business Media, 2008.
[45] W.-S. Fu, W.-J. Shieh, Transient thermal convection in an enclosure induced simultaneously by gravity and vibration, Int. J. Heat Mass Transf. 36 (2) (1993) 437–452, https://doi.org/10.1016/0017-9310(93)80019-Q.
[46] M. Ghalambaz, A.J. Chamkha, D. Wen, Natural convective flow and heat transfer of nano-encapsulated phase change materials (NEPCMs) in a cavity, Int. J. Heat Mass Transf. 138 (2019) 738–749, https://doi.org/10.1016/j.ijheatmasstransfer.2019.04.037.